Research
Microwave Wireless Power Transfer Technology—Article

An Approximate Analytical Method for a Slot Ring Radome

Kang Luo, Jin Meng *, Jiangfeng Han, Danni Zhu

National Key Laboratory of Electromagnetic Energy, Naval University of Engineering, Wuhan 430033, China

A B S T R A C T

In this paper, an in-band and out-of-band microwave wireless power-transmission characteristic analysis of a slot ring radome based on an approximate analytical method is proposed. The main contribution of this paper is that, in the approximate analysis of the ring radome, a unified expression of the incident field on the radome surface is derived with E-plane and H-plane scanning, and the ring is approximated as 30 segments of straight strips. Solving the corresponding 60×60 linear equations yields the electric current distribution along the ring strip. The magnetic current along the complementary slot ring is obtained by duality. Thanks to the fully analytical format of the current distribution, the microwave wireless power-transmission characteristics are efficiently calculated using Munk's scheme. An example of a slot ring biplanar symmetric hybrid radome is used to verify the accuracy and efficiency of the proposed scheme. The central processing unit (CPU) time is about 690 s using Ansys HFSS software versus 2.82 s for the proposed method.

© 2023 THE AUTHORS. Published by Elsevier LTD on behalf of Chinese Academy of Engineering and Higher Education Press Limited Company. This is an open access article under the CC BY-NC-ND license (http://creativecommons.org/licenses/by-nc-nd/4.0/).

1. Introduction

Radomes are periodic array structures that have been widely used in microwaves and antenna engineering to protect, isolate, and separate system signals from each other [1–4]. Radomes function as a spatial filter to block or transmit microwave wireless power with different frequency bands and scan angles. Among the various types of radomes, the ring loop is a typical element that has been extensively studied [5–11]. Parker and Hamdy [5] were the first to confirm that an array of simple rings can form a useful radome for a reflector antenna. The currents along the rings are expanded as a series of cosine and sine functions with several current modes. The transmission coefficients can be calculated using the usual modal procedure—namely, the moment method. For close lattice packing, the resonant frequency is relatively insensitive to the incidence angle and the scan plane. The ring loop radome was then extended to an array of concentric ring elements [6] and applied to a linearly polarized dual-band diplexer in an offset reflector [7]. The multiple layers can be analyzed using the equivalent circuit technique [8]. However, this modal procedure scheme cannot provide an immediate analysis of the electromagnetic properties of the radome. In recent years, rings have been

applied to absorbers and reconfigurable radomes. However, the transmission or reflection characteristics are still simulated using either commercial software [9,10] or the moment method [11].

Aside from numerical algorithms and the corresponding commercial software, approximate analytical methods provide an alternative approach. For example, the equivalent circuit method based on waveguide discontinuity has been widely applied to the approximate analysis of radomes [12,13], although this method is restrictive for certain structures (e.g., the square loop, square patch, and Jerusalem cross). To the best of our knowledge, the use of an equivalent circuit for a ring-type radome has not yet been reported. Other efficient approximate methods include the curve-fitting scheme [13] and the multimode network method [14]; however, these methods are based on a full wave simulation, which is time consuming. A promising approximate analytical method based on a Kirchhoff-type circuit and Munk's scheme has been proposed by some of the authors of this paper [15]. This method is efficient without requiring curve fitting and a full wave simulation. It also provides physical insight into the design.

However, few methods have been reported for determining the microwave wireless power-transmission characteristics of a slot ring radome, even though an increasing number of analysis methods and related applications of radomes are being investigated [16–19]. Three-dimensional (3D) numerical methods are somewhat inefficient, making it difficult to analyze the failure mechanism of a radome under high-power microwave irradiation

based on the physical concept. Although Munk's team [1] proposed the periodic moment method for a narrow strip/slot radome after rigorous mathematical and physical derivation, this method ignores the width effect of the strip/slot, and is still a full-wave numerical method with a large amount of computation. In particular, to determine the high-power microwave wireless transmission characteristics of a radome, it is necessary to analyze the location where the maximum electric field may exist, according to the structure of the radome elements [20,21].

In this paper, an approximate analytical method for slot ring radome analysis is proposed. First, according to the equivalent transmission line model, the ring is approximated by 30 segments of straight strips; it is then modeled by 30 sections of equivalent transmission lines (Section 2). Next, the associated magnetic current distribution is further applied to calculate the in-band filtering and breakdown characteristics (Section 3). Finally, the transmission characteristics of the out-band ultrawide-spectrum and narrow-spectrum high-power microwaves are analyzed (Section 4). Numerical examples and measurements are provided to verify the efficiency and accuracy of the proposed method.

2. Approximate analytical method

In this section, the tangential component of the electric field of the radome surface along the metal patch strip is deduced using E-plane and H-plane scanning to obtain a unified expression for calculating the current (i.e., magnetic current) distribution on the surface of a slot ring radome. Then, the ring is approximated as 30 segments of straight strips and modeled by 30 sections of equivalent transmission lines to calculate the power-transmission characteristics in Sections 3 and 4.

2.1. Tangential incident electric fields

A slot ring biplanar symmetric hybrid radome is depicted in Fig. 1 [1]. The E-plane is defined as the xy-plane, while the H-plane is defined as the yz-plane. As mentioned earlier, we first deduce the electronic current distribution along the ring strip shown in Fig. 2(a) and treat it as a patch-type radome complementary to the square slot ring in Fig. 1(b) exposed to an incident plane wave in the E/H plane, where $l = (a_1 + a_2) \sin(\pi/2N)$, l is the length of each of segment; a_1 and a_2 are the outside and inside diameters, respectively; and N is the number of segments. The magnetic current along the slot ring in Fig. 1(b) is then obtained by duality. Inspired by the mesh technology of commercial software, N segments of the end-to-end straight strips can be used to approximate
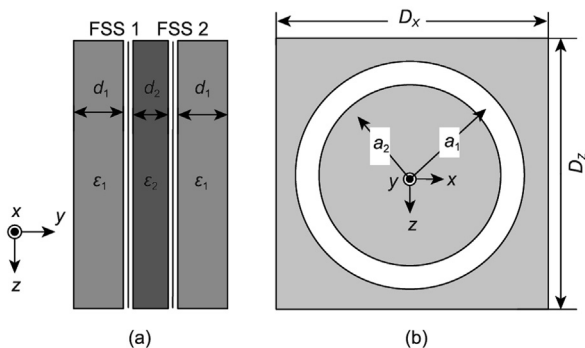

Fig. 1. Topology of a slot ring biplanar symmetric hybrid radome. (a) Side view; (b) top view of frequency selective surface (FSS). $\varepsilon_1 = 1.3$, $\varepsilon_2 = 1.9$, $d_1 = 9.0 \times 10^{-3}$, $d_2 = 5.5 \times 10^{-3}$, $a_1 = 3.500 \times 10^{-3}$, $a_2 = 3.375 \times 10^{-3}$, $D_x = D_z = 7.2 \times 10^{-3}$. ε_1, ε_2: the relative dielectric constant of outer and inner substrates, respectively; d_1, d_2: the thickness of outer and inner substrates, respectively; a_1, a_2: the outside and inside diameters, respectively; D_x, D_z: the length of the unit. Unit: meter.

a ring in terms of both visual and scattering characteristics. The local geometry is depicted in Fig. 2(a), together with the incident electric fields. The rings with different numbers of segments are shown in Fig. 2(b). It can be observed that the polygon formed by 30 segments can approximately model a ring.

The position coordinates of any point on each segment of the radome element are presented by a position vector. The origin of the coordinates ($\boldsymbol{R}^r = 0$) is defined as the reference point of the radome element. The vectors of the starting point and ending point corresponding to the ith segment are (x_{0i}, z_{0i}) and (x_{1i}, z_{1i}), respectively. It is assumed that the current reference directions of the element and the equivalent transmission line is $\boldsymbol{P}_i$:

$$\boldsymbol{P}_i = \frac{1}{l_i}[(x_{1i} - x_{0i})\boldsymbol{x} + (z_{1i} - z_{0i})\boldsymbol{z}] \tag{1}$$

where l_i is the length of each segment; $\boldsymbol{x}$ and $\boldsymbol{z}$ are unit vector along x and z axis, respectively.

The direction vector $\boldsymbol{S}$ and polarization direction $\boldsymbol{n}$ ($_\perp\boldsymbol{n}$ for vertical, $_\parallel\boldsymbol{n}$ for horizontal) of the incident wave can be expressed as follows:

$$\boldsymbol{S} = \sin\theta\boldsymbol{x} + \cos\theta\boldsymbol{y}, _\perp\boldsymbol{n} = \boldsymbol{z}, _\parallel\boldsymbol{n} = -\cos\theta\boldsymbol{x} + \sin\theta\boldsymbol{y} \tag{2}$$

where θ is the direction of incident wave and $\boldsymbol{y}$ is the unit vector along y axis.

According to Ref. [1], the tangential component of the incident electric fields can be rewritten as follows:

$$E_i^{\text{TE}}(\xi) = _\perp\boldsymbol{n} \cdot \boldsymbol{P}_i \cdot e^{-j\beta_0\boldsymbol{S}\cdot(x_{0i}\boldsymbol{x}+z_{0i}\boldsymbol{z}+\xi\boldsymbol{P}_i)} \tag{3}$$

$$E_i^{\text{TM}}(\xi) = _\parallel\boldsymbol{n} \cdot \boldsymbol{P}_i \cdot e^{-j\beta_0\boldsymbol{S}\cdot(x_{0i}\boldsymbol{x}+z_{0i}\boldsymbol{z}+\xi\boldsymbol{P}_i)} \tag{4}$$

where E^{TE} and E^{TM} are tangential component of the incident electric fields under transverse electric and magnetic wave, respectively; β_0 is the free space propagation constant; ξ is the measure of tangential component of the incident electric fields; j represents the imaginary part. When substituting Eqs. (1) and (2) into Eqs. (3) and (4), the following can be obtained:

$$E_i^{\text{TE}}(\xi) = \frac{z_{1i} - z_{0i}}{l_i} e^{-j\beta_0 \sin\theta x_{0i}} \cdot e^{-j\beta_0 \sin\theta \frac{x_{1i}-x_{0i}}{l_i}\xi} \tag{5}$$

$$E_i^{\text{TM}}(\xi) = -\cos\theta\frac{x_{1i} - x_{0i}}{l_i} e^{-j\beta_0 \sin\theta x_{0i}} \cdot e^{-j\beta_0 \sin\theta\frac{x_{1i}-x_{0i}}{l_i}\xi} \tag{6}$$

2.2. Current distribution

The one-wire equivalent transmission line model of Fig. 2(a) is shown in Fig. 2(c). The transmission line equations of the potential $V_i(z)$ and current $I_i(z)$ can be expressed as follows:

$$\frac{\partial V_i(z)}{\partial z} = -jwL_i \cdot I_i(z) + E_i(z) \tag{7}$$

$$\frac{\partial I_i(z)}{\partial z} = jwC_i \cdot V_i(z) \tag{8}$$

where

$$E_i(z) = \begin{cases} E_i^{\text{TE}}(\xi), & \text{TE wave} \\ E_i^{\text{TM}}(\xi), & \text{TM wave} \end{cases} \tag{9}$$

and where w is angular frequency; L_i and C_i are the equivalent inductance and capacitance of each segment, respectively.

The transmission line per unit length inductance can be calculated as follows:

$$L_i = \frac{\mu_0}{2\pi}\left[\ln\left(\frac{l_i}{\rho}\right) - 1\right] \tag{10}$$
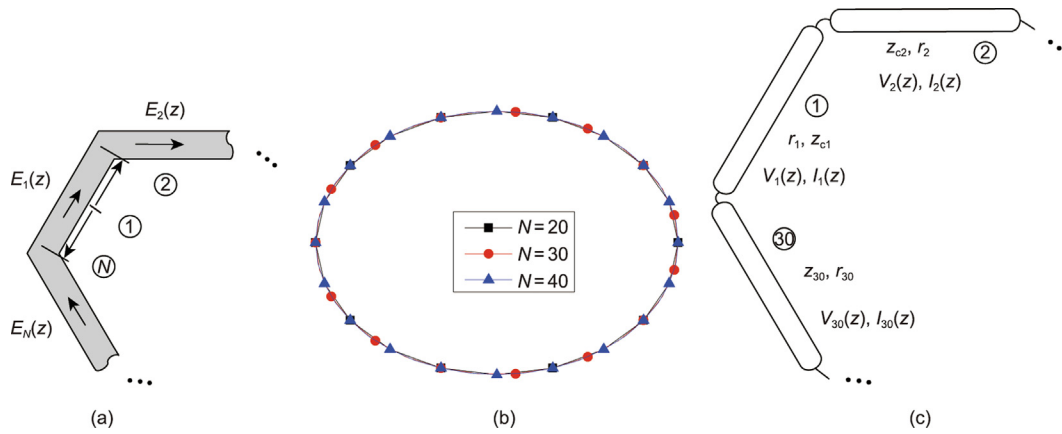
Fig. 2. Equivalent transmission line model. (a) Patch type radome complementary to the square slot ring; (b) rings with different numbers of segments; (c) one-wire lossy model. $E_1(z)$, $E_2(z)$, and $E_N(z)$: the tangential component of the incident electric fields; r_1, r_2, and r_{30}: the equivalent propagation constant of each segment; $V_1(z)$, $V_2(z)$, and $V_{30}(z)$: the potential along each segment; Z_{c1}, Z_{c2}, and Z_{30}: the equivalent impedance of each segment; $I_1(z)$, $I_2(z)$, and $I_{30}(z)$: the current along each segment.

where μ_0 is the free space permeability, and $\rho = (a_1 - a_2)/4$ is the equivalent radius of the microstrip line.

The characteristic impedance Z_{ci} and transmission constant r_i are as follows:

$$Z_{ci} = L_i/\sqrt{\mu_0 \varepsilon_0 \varepsilon_r}, r_i = j\omega\sqrt{\mu_0 \varepsilon_0 \varepsilon_r} \tag{11}$$

where $\varepsilon_r = (\varepsilon_1 + \varepsilon_2)/2$ is the equivalent of the relative permittivity; ε_1 and ε_2 are the relative dielectric constant of outer and inner substrates, respectively. ε_0 is the free space dielectric constant. Solving Eqs. (7) and (8) yields a general expression for the potential $V_i(z)$ and current $I_i(z)$, as follows:

$$V_i(z) = A_i e^{-r_i z} + B_i e^{r_i z} + \varphi_{vi}(z) \tag{12}$$

$$I_i(z) = \frac{1}{Z_{ci}}\left[A_i e^{-r_i z} - B_i e^{r_i z} + \frac{\varphi_i(z)}{r_i}\right] \tag{13}$$

where $\varphi_{vi}(z)$ and $\varphi_i(z)$ are the terms associated with the incident electric fields, and A_i and B_i are the coefficients to be solved. The current and potential boundary condition in Fig. 2(c) is as follows:

$$V_2(0) = V_1(l), I_2(0) = I_1(l); V_3(0) = V_2(l), I_3(0) = I_2(l); ...;$$
$$V_1(0) = V_{30}(l), I_1(0) = I_{30}(l) \tag{14}$$

By substituting Eqs. (12) and (13) into Eq. (14), a linear equation of 60×60 can be obtained. Solving this equation yields the corresponding coefficients in Eq. (13). The simulated current distributions are shown in Fig. 3.

For the E-plane scan, due to the use of a lossless equivalent transmission line model, as shown in Fig. 2(c), the real parts of the current approximate zero at a normal incident ($\theta = 0°$), as shown in Fig. 3(a). There is a maximum and a minimum point at the top and bottom sides of the ring for the image parts of the current. Two zero points are located at the left and right sides of the ring. This is a consequence of the symmetric structure and the tangential incident electric fields $E_i^{TE}(\xi)$.

Similarly, for the H-plane scan, the positions of the maximum point and the minimum point are exchanged due to the symmetric structure and source $E_i^{TM}(\xi)$, as shown in Fig. 3(b). The simulated current distributions at an obliquely incident ($\theta = 45°$) are shown in Figs. 3(c) and (d). The real part remains basically unchanged, while the imaginary part undergoes a reversal.

3. In-band transmission characteristics

Based on the current analysis calculated in Section 2, this section analyzes the in-band wireless power-transmission characteristics, including the in-band filtering characteristics (at a relatively low power) and the high-power microwave breakdown characteristics.

3.1. In-band filtering characteristics

As discussed in the introduction, the transmission coefficients of the radome in Fig. 1 can be calculated following Munk's scheme. The simulated results are plotted in Fig. 4, together with a comparison with the results obtained using Ansys HFSS (Ansoft, USA). The curves agree well with each other across a broad band. However, with an increase in the scan angle and frequency, the precision of the proposed scheme is reduced. Regardless, the proposed scheme is efficient without a full-wave analysis. The central processing unit (CPU) time is about 690.00 s for the proposed method, versus 2.82 s using Ansys HFSS. All calculations are performed on an Intel®Xeon® 2.80 GHz machine.

The typical method used to measure radome filtering characteristics is the window method, as shown in Fig. 5(a). The test scenario is shown in Fig. 5(b). By comparing the S_{12} parameters, which are measured by the vector network analyzer on the front and back of a radome placed in the window of the absorbing wall, the corresponding transmission characteristics can be calculated. There are 50×50 elements in Fig. 5(c), with a total size of 36 cm $\times$ 36 cm. The distance between the transmitting and receiving antennas is 2 m in Fig. 5(b) (about 73λ at the center frequency of 11 GHz, where λ is the wavelength of the unit). The measured in-band transmission coefficients are also plotted in Fig. 4. The transmitting and receiving antennas used for the test are consistent and can operate from 6 to 16 GHz. An Agilent N5230A PNA-L Network Analyzer (USA) was used to measure the transmittance S_{21}. As shown in Fig. 4, the curves agree well with each other. The error of the proposed method mainly results from the low precision of the transmission line parameters in the high-frequency band [21]. Based on the above analysis, this method has relatively high accuracy when the frequency is approximately 1.45 times lower than the center frequency and the inclination angle is less than 45°. In addition, the slot width should be no more than $0.025\lambda_0$, where λ_0 is the wavelength corresponding to the center frequency. Although there is a relatively large derivation, the
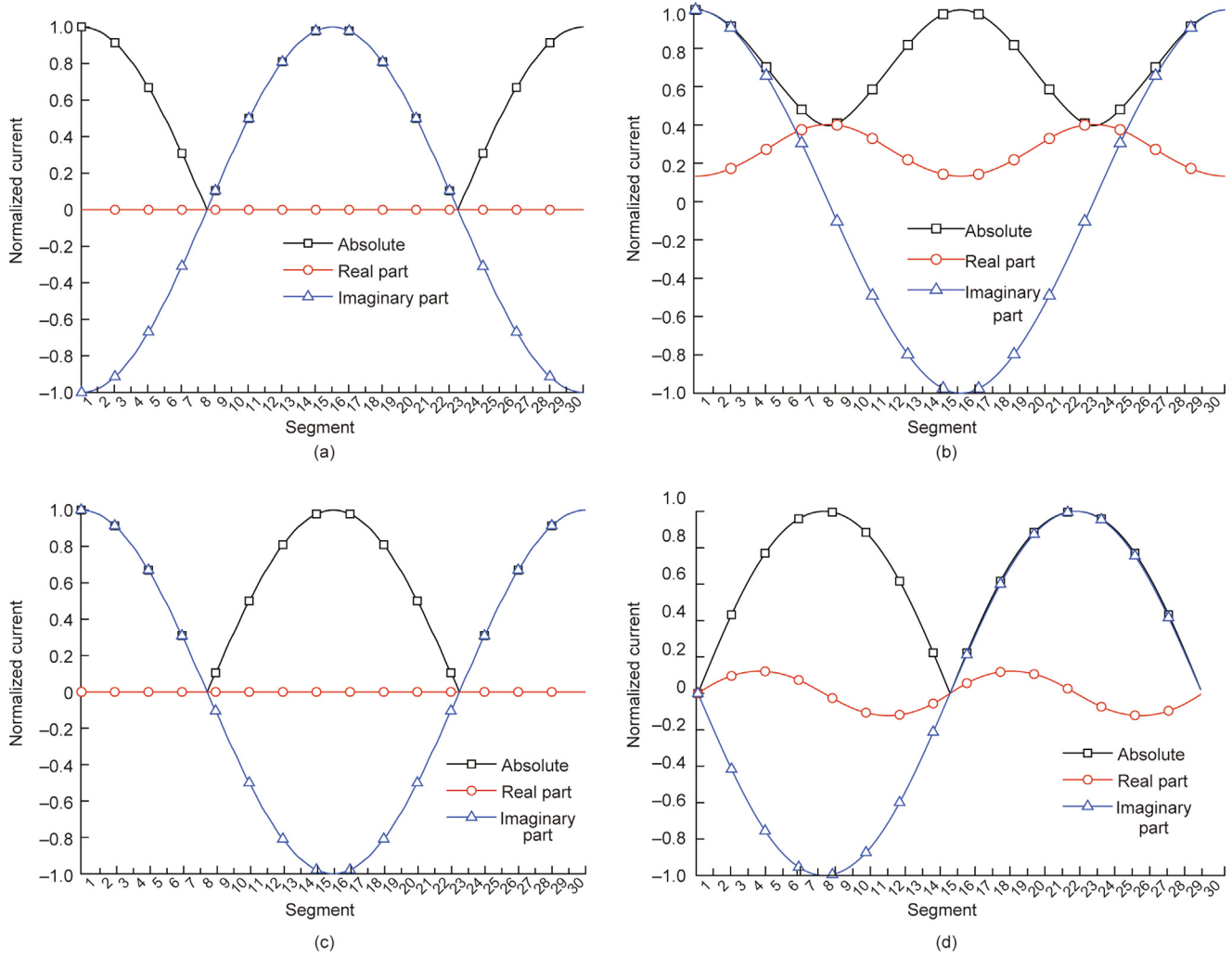
Fig. 3. Current distributions. (a) E-plane, $\theta = 0°$; (b) E-plane, $\theta = 45°$; (c) H-plane, $\theta = 0°$; (d) H-plane, $\theta = 45°$.

proposed method is efficient for a multilayered structure, with no need for curve fitting or a full-wave simulation.

3.2. In-band breakdown characteristics

The in-band breakdown characteristics of a wireless high-power microwave radome can usually be evaluated by the maximum electric field that it can withstand. The calculation accuracy of the maximum electric field of the radome element depends on a reasonable approximation of the equivalent transmission line model. The magnetic current distribution function calculated in Section 2 can be further used to calculate the maximum electric field in this section.

It can be observed from Ref. [1] that the real part of the scanning admittance of the radome element under resonance conditions (G_A) is as follows:

$$G_A = \frac{4Y_0}{D_x D_z} \cdot \frac{1}{r_y} \cdot \left[{}_\perp P_0 \cdot {}_\perp P_0^t + {}_\parallel P_0 \cdot {}_\parallel P_0^t \right] \tag{15}$$

where D_x and D_z are the lengths of the unit, Y_0 is the free space wave admittance, and r_y is the phase velocity of the array plane; ${}_\perp P_0$ and ${}_\perp P_0^t$ represent the vertical receiving and transmitting functions, respectively; and ${}_\parallel P_0$ and ${}_\parallel P_0^t$ represent the horizontal receiving and transmitting functions, respectively.

$$ {}_\parallel P_0 = {}_\parallel \boldsymbol{n}_0 \cdot \boldsymbol{p}^{(0)} \int_{\text{element}} I(l) e^{j\beta_0 l \boldsymbol{p}^{(0)} \boldsymbol{r}_0} \mathrm{d}l \tag{16}$$

$$ {}_\parallel P_0^t = {}_\parallel \boldsymbol{n}_0 \cdot \boldsymbol{p}^{(0)} \int_{\text{element}} I^t(l) e^{j\beta_0 l \boldsymbol{p}^{(0)} \boldsymbol{r}_0} \mathrm{d}l \tag{17}$$

where $\boldsymbol{p}^{(0)}$ is the reference direction; ${}_\parallel \boldsymbol{n}_0$ is the wave vector reference direction; $\boldsymbol{r}_0$ is the plane spectrum direction; and $I(l)$ and $I^t(l)$ are the receiving and transmitting current distribution functions, respectively [1]. According to Galerkin, $I(l)$ and $I^t(l)$ are similar to the basis functions and test functions, respectively; that is, they can be replaced by those calculated in Section 2.

The slot array is usually used to analyze the incident magnetic field H^i, and the induced current I^i is as follows:

$$I^i = 2 \left[{}_\perp H^i \cdot {}_\perp P_0^t + {}_\parallel H^i \cdot {}_\parallel P_0^t \right] \tag{18}$$

Then, the maximum port voltage $V_{B,\max}$ is as follows:

$$V_{B,\max} = I^i / G_A \tag{19}$$

The maximum field $E_{B,\max}$ of the slot type radome element is as follows:
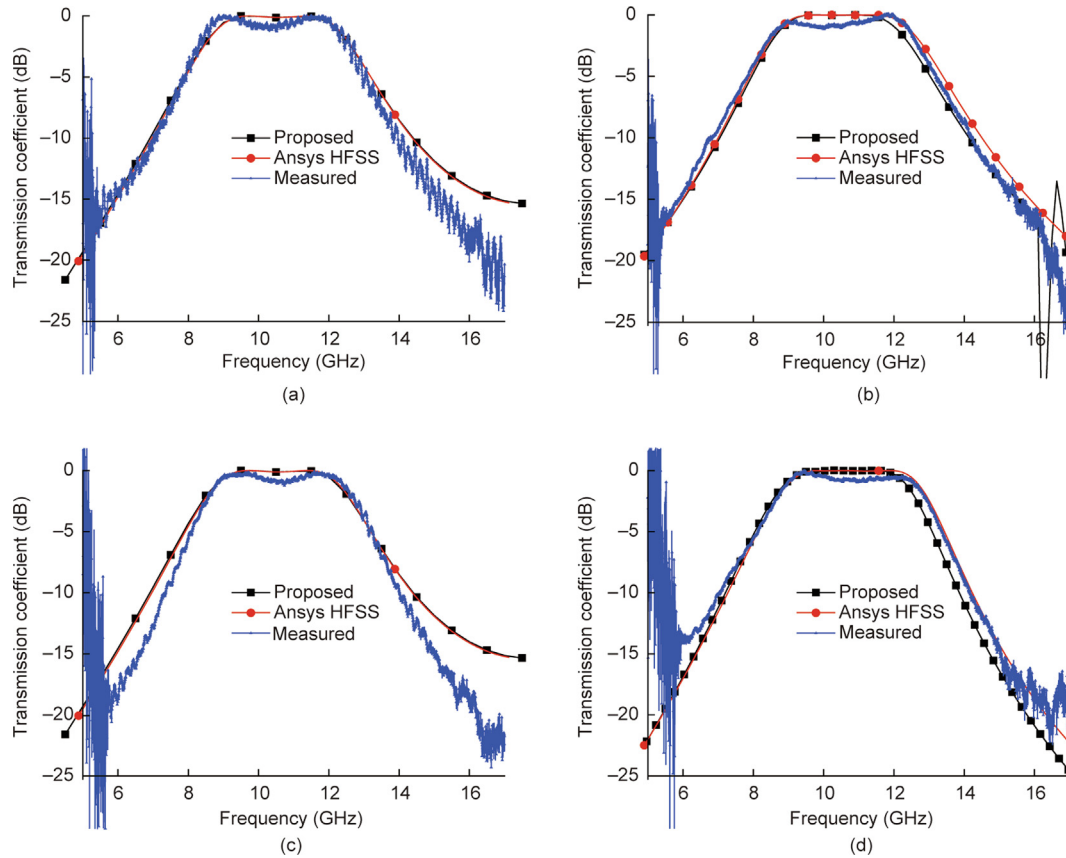
$$E_{B,\max} = \alpha \frac{V_{B,\max}}{w} \tag{20}$$

Fig. 4. Transmission coefficients. (a) E-plane, $\theta = 0°$; (b) E-plane, $\theta = 45°$; (c) H-plane, $\theta = 0°$; (d) H-plane, $\theta = 45°$.
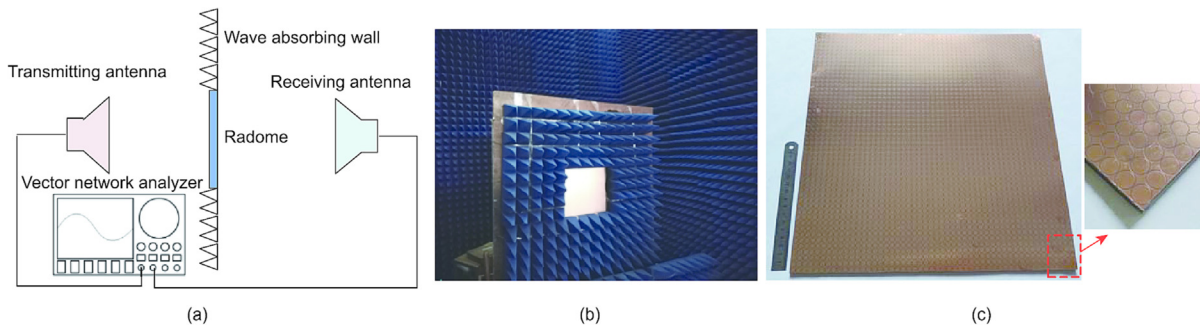

Fig. 5. Measurement of the transmission coefficients. (a) Test diagram; (b) test scenario; (c) fabricated protype.

where α is the shape factor. To facilitate a comparison with the HFSS electromagnetic simulation results, the average power of the incident electromagnetic wave in Fig. 1 is set as 1 W, and the corresponding incident magnetic field intensity is as follows:

$$H^i = \sqrt{\frac{1}{\eta_0 D_x D_z}} \qquad (21)$$

where η_0 is the free space wave impedance. Based on Fig. 3, the corresponding position of the maximum magnetic current is shown in Fig. 6(a). These two points are the positions of the maximum voltage, as shown in Fig. 6(b). The current distribution calculated by Eqs. (12)–(14) is introduced into Eqs. (16) and (17) to calculate the shape function; then, the element scanning admittance is calculated by means of Eq. (15) in order to finally calculate the maximum electric field of the element, which is 41.2 kV·m^{-1}. To verify the

correctness of this method, Ansys HFSS is used to simulate the slot electric field in Fig. 1. As shown in Fig. 6(b), the maximum electric field is 47.6 kV·m^{-1}. The value and position of the maximum electric field are approximately consistent with those obtained using the proposed method, which verifies the effectiveness of the proposed method.

4. Out-of-band transmission characteristic

Aside from the analysis of the in-band filtering characteristics, the analysis of the out-band filtering characteristics of the radome is also important. Under high-power microwave irradiation, if the shielding efficiency of the radome against the microwave wireless power is low, saturation of the low-noise amplifier at the radio frequency (RF) front end will occur, which will affect the
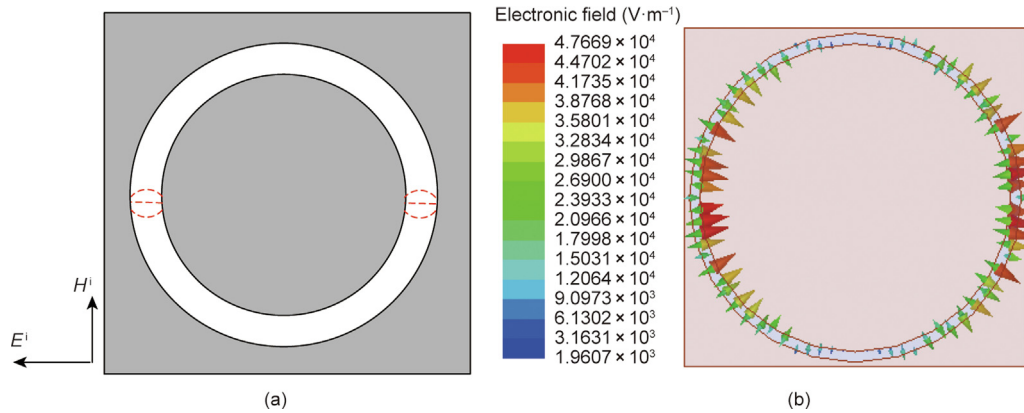
Fig. 6. Breakdown characteristics. (a) Electric field breakdown diagram; (b) simulated slot electric field distribution by means of Ansys HFSS.

signal-to-noise ratio of the received signal and may even burn the back-end digital circuit board. In particular, when the radome is damaged, the in-band filtering characteristics will be ineffective, causing the spatial filtering function to be lost. This section further investigates the out-band filtering characteristics of a radome under the irradiation of an ultrawide-spectrum and narrow-spectrum wireless high-power microwaves.

4.1. Transmission characteristics of an out-band ultrawide-spectrum high-power microwave

The time domain waveform $E(t)$ of an ultrawide-spectrum high-power microwave can be approximated by the differential Gaussian pulse, as follows:

$$E(t) = E_0 \frac{t - t_0}{\tau} \exp\left[-\frac{4\pi(t - t_0)}{\tau^2}\right] \tag{22}$$

where E_0 is the magnitude, t_0 is the delay, t is the time measure of the time domain waveform, and τ is the pulse width. The frequency domain form $E(f)$ after a Fourier transform is as follows:

$$E(f) = -\frac{jE_0\tau^2 f}{8} \exp\left[-2\pi j f t_0 - \frac{\pi f^2 \tau^2}{4}\right] \tag{23}$$

where f is the frequency corresponding to Fourier transform.

It can be observed from Eqs. (22) and (23) that the time domain waveform and spectrum are related to τ. The smaller τ is, the narrower the pulse is and the wider the spectrum will be.

According to the current development status of high-power microwaves, the spectrum of an ultrawide-spectrum high-power microwave is mainly concentrated in the range of 0.15–5.00 GHz, and microwaves with higher frequencies may be developed in the future. Therefore, in our investigation of the out-of-band filtering characteristics of an ultrawide-spectrum high-power microwave, three typical time-domain waveforms are taken as examples, and the values of τ are selected to be 4×10^{-9}, 4×10^{-10}, and 4×10^{-11}. In this case, when $\tau = 4 \times 10^{-9}$ and $\tau = 4 \times 10^{-10}$, the pulse spectrum covers the frequency band below 5 GHz, which corresponds to the frequency range of the ultrawide-spectrum high-power microwave at present. When $\tau = 4 \times 10^{-11}$, the pulse spectrum is as high as 60 GHz, which can represent the development trend of ultrawide-spectrum high-power microwaves in the future. Although the spectrum is wide, making it difficult to realize technically, and although it covers the working frequency band of the radome, a theoretical discussion on its filtering characteristics is beneficial to improve the comprehensive performance.

The three ultrawide-spectrum high-power microwaves described above are irradiated onto the radome shown in Fig. 1

as incident waves, and the out-of-band filtering characteristics are analyzed. Fig. 7(a) shows the time domain waveform of the transmitted field through the radome when $\tau = 4 \times 10^{-9}$. The transmission field is very small, which confirms that the peak attenuation of the incident wave is about 54.9 dB. This is because the spectrum of the incident wave is far lower than the pass band of the radome, and the out-of-band filtering characteristics are good, so the transmission field is very small. Fig. 7(b) shows the time-domain waveform of the transmitted field transmitted through the radome when $\tau = 4 \times 10^{-10}$. It can be seen that the transmitted field is also very small, and the peak attenuation of the incident wave by the radome reaches 30.5 dB. The reason for this is because this situation is similar to that when $\tau = 4 \times 10^{-9}$. Fig. 7(c) shows the time-domain waveform of the field transmitted through the radome when $\tau = 4 \times 10^{-11}$. Although the incident wave spectrum covers the pass band, it still has a large attenuation of the pulse peak at 14.4 dB. This is because the radome has good out-of-band filtering characteristics, and only the frequency component overlapping with the passband in the incident pulse can pass through it. Therefore, the peak value of the pulse wave still has a large attenuation.

The research described above on the out-of-band filtering of an ultrawide-spectrum high-power microwave by a radome shows that the radome has a strong attenuation inhibition effect on an ultrawide-spectrum high-power microwave with various waveforms. The lower the frequency of the incident wave, the stronger the attenuation. Even if the ultrawide-spectrum high-power microwave spectrum covers the passband of the radome, it still has a peak attenuation of about 15 dB. This finding confirms that the radome has good out-of-band filtering characteristics for an ultrawide-spectrum high-energy electromagnetic pulse.

4.2. Transmission characteristics of an out-band narrow-spectrum high-power microwave

A narrow-band high-power microwave is a high-power electromagnetic pulse with a carrier frequency. Its frequency band is relatively narrow, typically tens of megahertz. Its time-domain waveform is a pulse-modulated sine wave, which can be approximately expressed by the following formula:

$$E(t) = \begin{cases} E_0 \frac{t}{t_1} \sin(2\pi f_0 t), & t < t_1 \\ E_0 \sin(2\pi f_0 t), & t_1 < t < t_1 + \tau \\ E_0 \left(\frac{\tau + t_1}{t_1} - \frac{t}{t_1}\right) \sin(2\pi f_0 t), & t_1 + \tau < t < t_1 + 2\tau \\ 0, & \text{others} \end{cases} \tag{24}$$
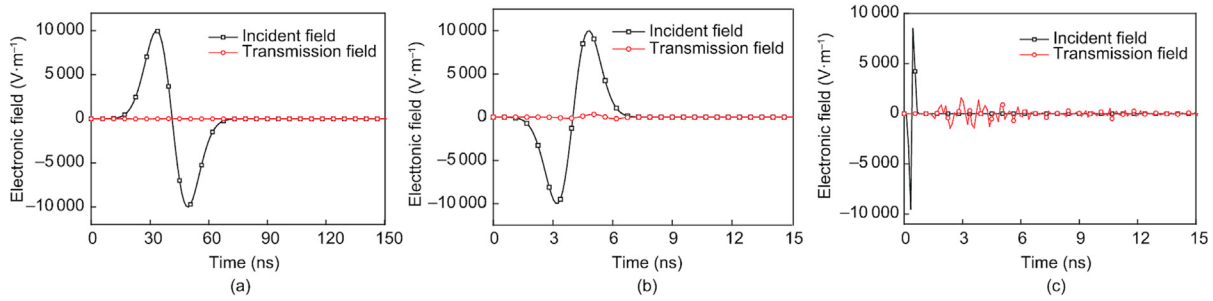
Fig. 7. Ultrawide-band pulse spectrum and transmission time domain waveform of the radome under irradiation. (a) $\tau = 4 \times 10^{-9}$; (b) $\tau = 4 \times 10^{-10}$; (c) $\tau = 4 \times 10^{-11}$.
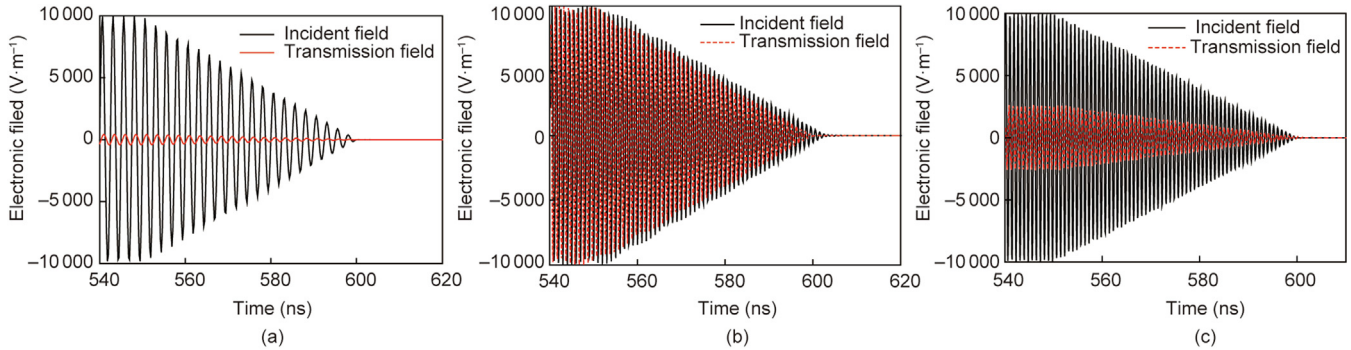

Fig. 8. Narrow-band pulse spectrum and transmission time domain waveform of the radome under irradiation. (a) $f_0 = 6$ GHz; (b) $f_0 = 11$ GHz; (c) $f_0 = 16$ GHz.

where t_1 represents the rising and falling edges of the modulation pulse, and f_0 is the carrier frequency. The same modulation pulse is selected, $t_1 = 5$ ns and $\tau = 50$ ns are set, and the three carrier frequencies of 6, 11, and 16 GHz are selected.

Fig. 8 shows the incident wave and transmitted wave when the radome is irradiated with three carrier frequencies. The simulation results show that, when $f_0 = 11$ GHz, most of the incident narrowband high-power microwaves can pass through the radome, and the corresponding shielding efficiency is 0.01 dB. This is because the frequency band of the narrowband high-power microwaves is within or near the passband. For the other two cases, it can be seen in Figs. 8(a) and (c) that almost all the incident waves are reflected after being irradiated to the radome. Moreover, as the narrow-band high-power microwave frequency moves away from the passband, the transmission part is obviously smaller, and the corresponding shielding effectiveness is –18.5 and –14.6 dB. Therefore, the radome in Fig. 1 has good out-of-band filtering characteristics for narrow-band high-power microwaves.

In the above simulation, the maximum peak electric field of the irradiated sample is 2.0×10^5 V·m^{-1}. If the maximum field enhanced factor of the sample is 45 [20], the maximum peak electric field in the sample gap is about 45 times greater than the peak electric field of the irradiated wave, at 9.0×10^6 V·m^{-1}. This is far lower than the critical field strength of the sample medium (2.0×10^7–3.0×10^7 V·m^{-1}). The dielectric critical field strength is the breakdown threshold of the electrostatic field or continuous field, while the high-power microwave source is a narrow pulse with a pulse width of only 4 ns. Therefore, the critical field strength of the high-power microwave should be much higher than that of the electrostatic field, making it impossible for the field to break down in the test. Even if the maximum field enhanced factor of the sample is calculated as 100, the maximum peak electric field in the sample gap is only 2.0×10^7 V·m^{-1}, which just reaches the critical field strength range of the medium. As mentioned above, because the pulse width of the high-power microwave source is very narrow, it is impossible to break the field down.

5. Conclusions

In this paper, an approximate analytical method for the microwave wireless power-transmission characteristics of a slot ring radome was proposed. In the proposed method, the magnetic current along the slot ring is obtained by the duality of the electronic current along the complementary strip ring. The strip ring is approximated by 30 segments of straight strips, each of which is modeled as a Kirchhoff-type circuit. According to the Kirchhoff current law and the continuity condition for the potential, a matrix equation of 60×60 is established. Once the current is solved, the in-band and out-of-band microwave wireless power-transmission characteristics can be calculated following Munk's scheme. The proposed method is more efficient than using Ansys HFSS software.

Compliance with ethics guidelines

Kang Luo, Jin Meng, Jiangfeng Han, and Danni Zhu declare that they have no conflict of interest or financial conflicts to disclose.

References

[1] Munk BA. Frequency selective surfaces: theory and design. New York City: Wiley; 2000.

[2] Zhu X, Wu LS, Guo YX, Wu W. Tunable graphene FSS for terahertz applications. In: Proceedings of IEEE Antennas and Propagation Society International Symposium; 2014 Jul 6–11; Memphis, TN, USA; 2014.

[3] Gao X, Han X, Cao WP, Li HO, Ma HF, Cui TJ. Ultrawideband and high-efficiency linear polarization converter based on double V-shaped metasurface. IEEE Trans Antennas Propag 2015;63(8):3522–30.

[4] Sabri L, Amiri N, Forooraghi K. Dual-band and dual-polarized SIW-fed microstrip patch antenna. IEEE Antennas Wirel Propag Lett 2014;13:1605–8.

[5] Parker EA, Hamdy SMA. Rings as elements for frequency selective surfaces. Electron Lett 1981;17(17):612–4.

[6] Parker EA, Hamdy SMA, Langley RJ. Arrays of concentric rings as frequency selective surfaces. Electron Lett 1981;17(23):880–1.

[7] El-morsy MAA, Parker EA. A linearly-polarized dual-band diplexer in an offset reflector. J Inst Electron Radio Eng 1986;56(3):111–6.

[8] Parker EA, Vardaxoglou JC. Influence of single and multiple-layer dielectric substrates on the band spacings available from a concentric ring frequency-selective surface. Int J Electron 1986;61(3):291–7.

[9] Sakran F, Neve-Oz Y, Ron A, Golosovsky M, Davidov D, Frenkel A. Absorbing frequency-selective-surface for the mm-wave range. IEEE Trans Antennas Propag 2008;56(8):2649–55.

[10] Sanz-Izquierdo B, Parker EA. Dual polarized reconfigurable frequency selective surfaces. IEEE Trans Antennas Propag 2014;62(2):764–71.

[11] Kazantsev YN, Lopatin AV, Kazantseva NE, Shatrov AD, Mal'tsev VP, Vilčáková J, et al. Broadening of operating frequency band of magnetic-type radio absorbers by FSS incorporation. IEEE Trans Antennas Propag 2010;58 (4):1227–33.

[12] Marcuvitz N. Waveguide handbook. New York City: McGraw; 1951.

[13] Costa F, Monorchio A, Manara G. Efficient analysis of frequency selective surfaces by a simple equivalent-circuit model. IEEE Antennas Propag Mag 2012;54(4):35–48.

[14] Mesa F, García-Vigueras M, Medina F, Rodríguez-Berral R, Mosig JR. Circuit-model analysis of frequency selective surfaces with scatterers of arbitrary geometry. IEEE Antennas Wirel Propag Lett 2015;14:135–8.

[15] Luo K, Yi Y, Zong ZY, Chen B, Zhou XL, Duan YT. Approximate analysis method for frequency selective surface based on Kirchhoff type circuit. IEEE Trans Antennas Propag 2018;66(11):6076–85.

[16] Schelkunoff SA, Friis HT. Antennas theory and practice. New York City: Wiley; 1952.

[17] Zhang JH, Lin MT, Wu Z, Ding L, Bian L, Liu P. Energy selective surface with power-dependent transmission coefficient for high-power microwave protection in waveguide. IEEE Trans Antennas Propag 2019;67(4):2494–502.

[18] Zhao C, Wang CF, Aditya S. Power-dependent frequency-selective surface: concept, design, and experiment. IEEE Trans Antennas Propag 2019;67 (5):3215–20.

[19] Li X, Zhou Z, Wang Q, Zhang J. A polarization conversion radome for high-power microwave applications. IEEE Antennas Wirel Propag Lett 2019;18 (6):1096–9.

[20] Zhou X, Luo K, Chen B, Wang Y. Simulation analysis of frequency selective surface with high power handing capability. In: Proceedings of the 7th Asia-Pacific Conference on Environmental Electromagnetics; 2015 Nov 4–7; HangZhou, China; 2015.

[21] Luo K, Meng J, Zhu DN, Ge SH, Han JF. Approximate analysis method for hexagonal slot frequency selective surface analysis. Int J RF Microw Comput-Aided Eng 2021;31(9):e22776.